

Numerical Study of a Transonic Wingtip Flow

J.R. Grisham, F.K. Lu, and B.H. Dennis

*Mechanical and Aerospace Engineering Department,
University of Texas at Arlington, Arlington, Texas, USA*

INTRODUCTION

Although transonic flight is now commonplace, new, unconventional designs are being proposed and evaluated. As such, transonic testing is still a topic of interest. One type of test facility that allows transonic flows at high Reynolds numbers is a Ludwieg tube tunnel. These tunnels have short test times of about 0.1 s. While force measurements have proceeded in a conventional manner, recent developments in dynamic force measurements in hypersonic shock tunnels have led the same principles to be applied on a transonic NACA 0012 wingtip⁽¹⁾. The force measurements were corrected for dynamic effects arising from stress waves propagating through the model/balance structure. The purpose of the present work is to validate the experimental force coefficients via numerical simulations. Additionally, a qualitative comparison between experimental and numerical surface flow visualization will be provided.

EXPERIMENTAL BACKGROUND

Amongst smallscale specialized wind tunnels is the pilot HIRT^a or HIRT for short⁽²⁾. The pilot HIRT was decommissioned in 1976 and donated to the University of Texas at Arlington in 1978. Ludwieg tubes are short duration facilities, typically with run times of a few hundred milliseconds. Due to the short run time, there are concerns lately that the dynamic loading of force balances may affect measurements⁽³⁾. Development in the understanding of the influence of system dynamics on force measurements spanned a number of decades, driven primarily by shock tunnel applications; see Ref. 3 for a discussion. These developments along with the concern that the dynamics of the wind tunnel was affecting the force measurements led to the work of Werling, et al⁽¹⁾.

The HIRT is shown schematically in Fig. 1. As can be seen from the figure, the general features of a Ludwieg tube are similar to the more familiar supersonic blowdown tunnel, possessing a nozzle to raise the Mach number, a test section and a diffuser. The test section is 186 mm high by 232 mm wide by 635 mm long (7.75×9×25 in.). It can be surrounded by four porous sides, or have porous top and bottom with solid side walls. The current results are of the later configuration. The purpose of porous walls is to allow air to be vented to ensure that shocks that impinge upon these surfaces do not reflect back into the test section. Figure 2 shows the test article, which is a wingtip with a NACA 0012 profile, mounted onto a sidewall balance. The operation of the balance is omitted for brevity⁽¹⁾.

To reveal the footprint of flow features, surface flow visualization utilizing a mixture of light transmission oil and powdered fluorescent chalk was employed⁽⁴⁾. Through trial-and-error, it

^aHigh Reynolds number Transonic wind tunnel

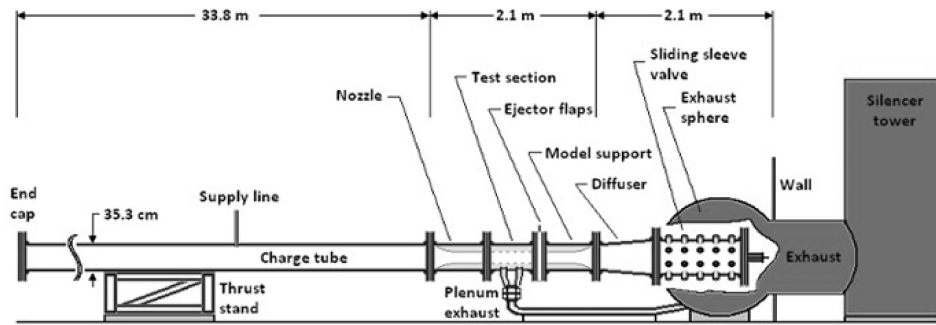


Figure 1: Schematic of Ludwieg tube.



Figure 2: View upstream of Ludwieg tube showing the wall-mounted wing tip.

was found that chalk particles of up to 100 microns in size are suitable in not interfering with the flow and yet produce streaks that enhance the visualization. The mixture was applied over the entire surface of the wingtip. After a run, the entire model is removed from the test section and photographed under ultraviolet light.

NUMERICAL METHOD

NASA's FUN3D flow solver was used to numerically solve the Navier-Stokes equations⁽⁵⁾. The turbulence model used was the Spalart-Allmaras model. Feature-based refinement along with a mesh study were used to ensure a mesh-independent solution.

The meshes were generated using Pointwise and AFLR3^(6,7). Specifically, a script was written to generate the geometry and surface meshes in Pointwise. The surface mesh was then input to AFLR3 for volume mesh generation. Fig. 3 shows the mesh on the upper surface of the wing and the geometry (with upper, lower and closest walls not shown for clarity). Before adaptation, each mesh consisted of approximately 6.3 million nodes and 37 million tetrahedral cells. The mesh was frozen below $y^+ \approx 300$ so that boundary layer resolution was maintained throughout the adaptation.

The feature-based mesh adaptation process involves two main steps, namely, computation of a metric that represents the desired cell size and adaptation of the mesh to achieve the desired result. In this work, the flowfield variable used to compute the metric was the Mach number. A Hessian matrix is then formed using a least-squares gradient calculation. This Hessian matrix is used to stretch the mesh and the scalar flowfield variable is used to determine the isotropic spacing^(8,9). Some sample results of the adaptation applied to this configuration can be seen in Fig. 4. Furthermore, the mesh adaptation improved the residual convergence of the flow solver while also decreasing the number of grid points. After adaptation, each mesh consisted

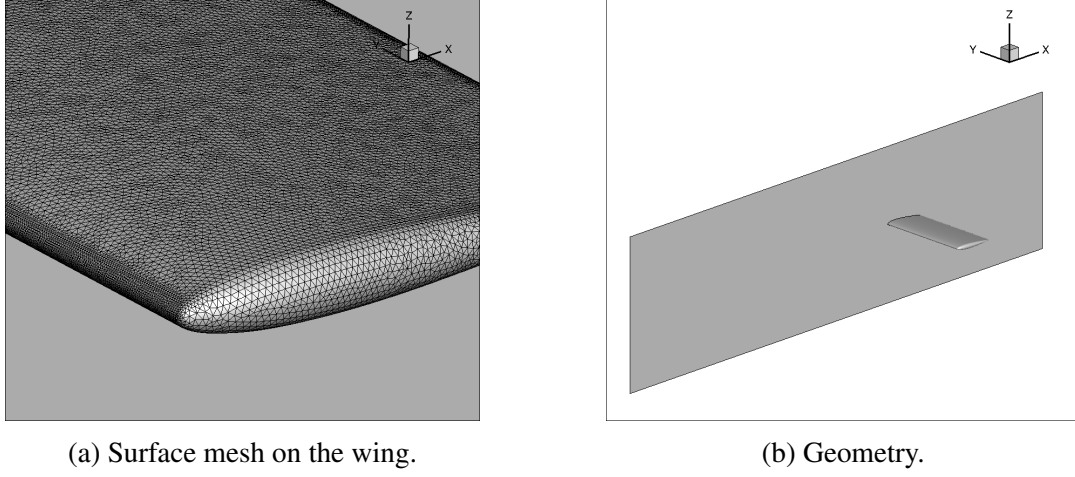


Figure 3: Geometry and surface mesh.

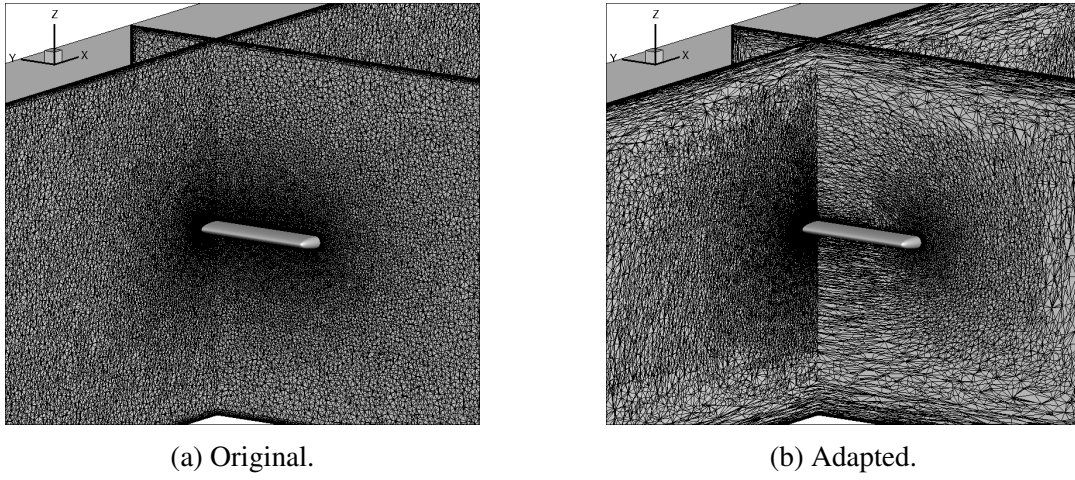


Figure 4: Comparison between original and refined meshes.

of approximately 4.5 million nodes and 27 million tetrahedral cells.

RESULTS AND DISCUSSION

Figure 5 shows comparisons between force coefficients in the form of lift coefficient vs angle of attack and a drag polar. The force coefficients are defined as follows:

$$C_L = \frac{L}{q_\infty S} \quad (1a)$$

$$C_D = \frac{D}{q_\infty S} \quad (1b)$$

$$q_\infty = \frac{1}{2} \rho_\infty V_\infty^2 \quad (1c)$$

where L , D , q_∞ , and S represent the lift force, drag force, freestream dynamic pressure and planform area, respectively. Harris' two-dimensional results at $M = 0.74$ and $Re = 3 \times 10^6$ are also shown⁽¹⁰⁾. A close examination of Fig. 5a reveals that the lift coefficient values closely follow the experimental values. Both, the experimental and computational results show less lift generation than Harris' two-dimensional case at the same incidence angle. This is to be

expected from classical aerodynamics theory since the finite aspect ratio of the wing tip induces a downwash that effectively reduces the angle of attack. The comparison in Fig. 5b shows that the computations and experiment agree well for negative angles of attack. There is less agreement between the computations and experiments at positive angles of attack. Furthermore, the experimental lift coefficient does not equal zero at zero angle of attack. These discrepancies could be because of a slight error in experimentally measured angles of attack.

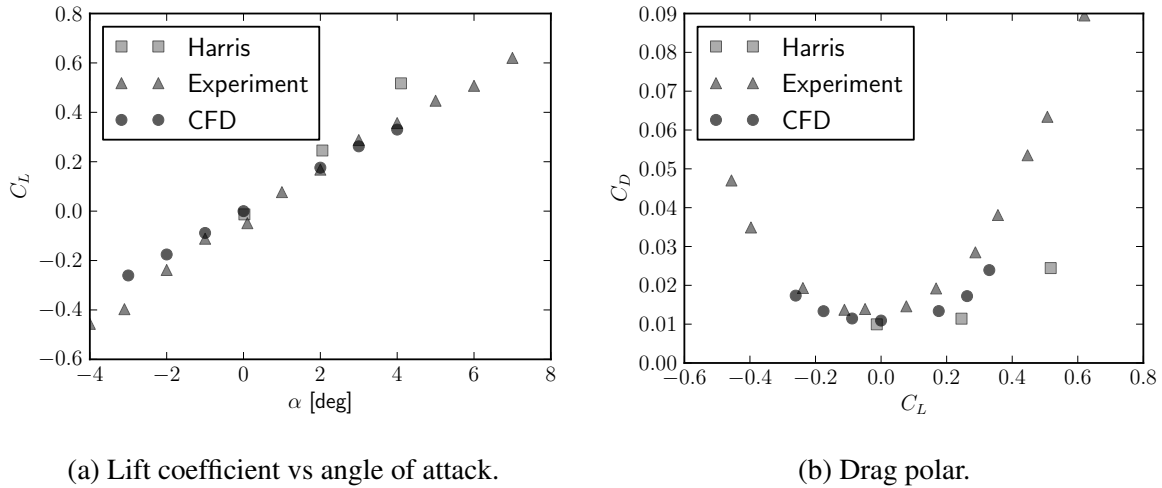


Figure 5: Comparison between force coefficients.

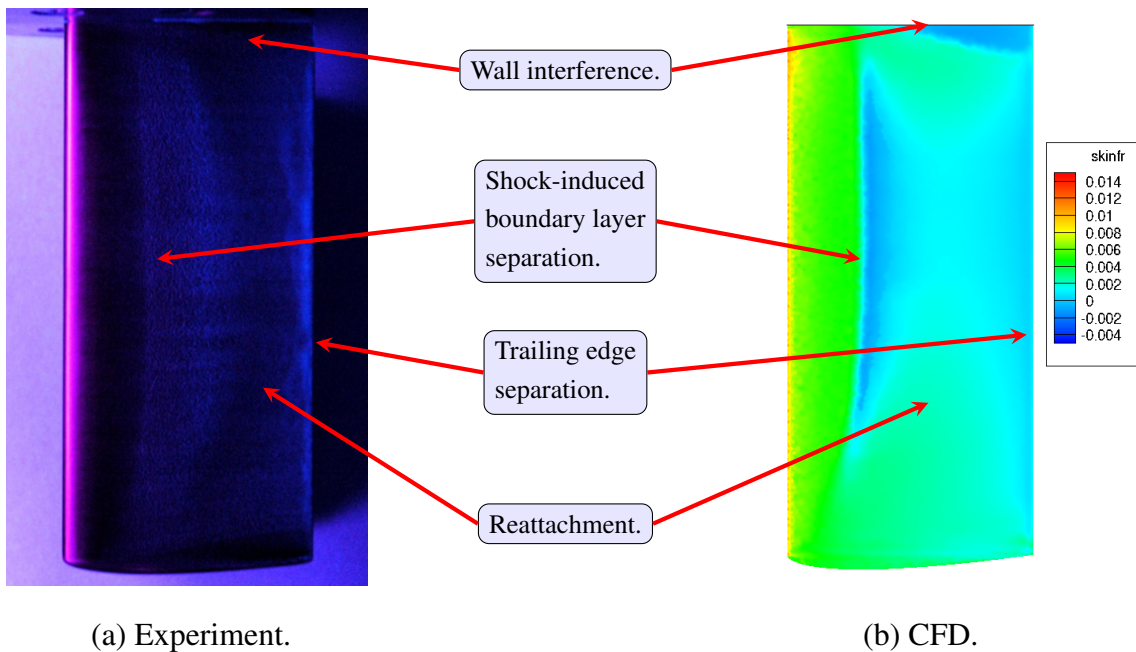


Figure 6: Comparison between experimental and computational surface flow visualization at $\alpha = 4^\circ$ (top view).

Figure 6 shows a comparison between experimental and computational surface flow visualization. Prior to these computations, the experimental surface flow visualization and the flowfield itself were not well-understood. By comparing the experimental and computational results, several of the major flow features are elucidated. The flow is from right to left in both

cases. Proceeding in the streamwise direction, the first major feature is shock-induced boundary layer separation. This shows up on the experimental SFV as a bright region, most likely because of the reduced scouring of the fluorescent mixture in the slow recirculating flow of the separation bubble. After the shock-induced separation, the flow reattaches, followed by further separation on the trailing edge of the wing. This trailing edge separation also shows up as a bright region on the experimental SFV. These regions can be identified from the computational data by locating regions in which the skin friction coefficient is negative.

Another feature that is not well-understood is the wall interference. To better understand this, streamlines were placed near the junction between the wing and the sidewall. The result can be seen in Fig. 7. Although the shock is significantly weakened by the time it reaches the wall, an adverse pressure gradient is still imposed on the sidewall boundary layer and the boundary layer on the surface of the wing. This adverse pressure gradient along with turning the flow away from itself are responsible for creating separated flow in this region. The turning affects the flow in this way because of the inertia of the fluid. This separation creates cross flows on the sidewall and the surface of the airfoil. Specifically, the flow along the side wall is deflected upward and the flow along the surface of the airfoil is deflected outward away from the sidewall.

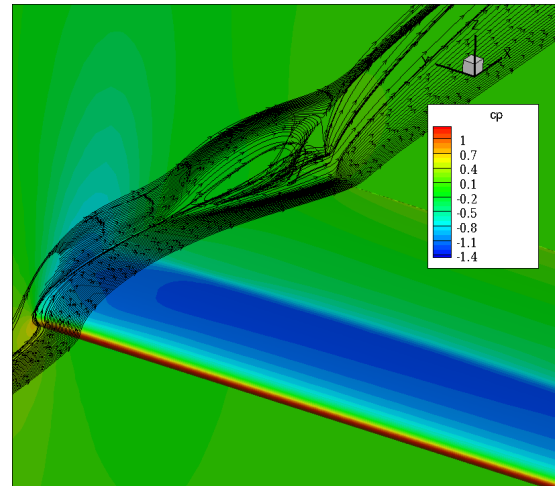


Figure 7: Streamlines at junction between wing and sidewall with contours of pressure coefficient.

CONCLUSIONS

A numerical study of a NACA 0012 wingtip was presented. The study included a comparison with experiments which involved novel methods for force measurements, namely, a dynamic calibration meant to compensate for stress waves propagating through the tunnel. A comparison between the force coefficients for different angles of attack was presented and shows good agreement. Surface flow visualizations from the experiment and computations were compared and new light was shed on several of the major features in the flow as a result of the CFD data. The comparison presented here suggests that the dynamic calibration used to compensate for short run times was effective. This comparison also demonstrates the feasibility of using more complex models for calibrating wind tunnels in concert with CFD

ACKNOWLEDGEMENTS

The authors would like to thank the FUN3D team for answering questions about operating the code, and Pointwise and the SimCenter at Mississippi State University for the use of their meshing software. The computations were performed using high performance computing resources at the Texas Advanced Computing Center.

References

1. Werling M, Gutierrez J, Braun E, and Lu F, *Force measurements on a NACA 0012 wingtip at Mach 0.75*. AIAA 2013-1026, AIAA (2013).
2. Starr RF and Schueler CJ, *Experimental studies of a Ludwieg tube high Reynolds number transonic tunnel*. AEDC TR 73-168 (1973).
3. Juhany KA and Darji A, *Force measurement in a Ludwieg tube tunnel*. Journal of Spacecraft and Rockets 44(1), 88–93 (2007).
4. Knight KCD, Braun EM, Roy CJ, Lu FK, and Schetz JA, *Interference drag modeling and experiments for a high-Reynolds-number transonic wing*. Journal of Aircraft 49(6), 1894–1903 (2012).
5. Biedron RT, Derlaga JM, Gnoffo PA, Hammond DP, Jones WT, Kleb B, Lee-Rausch EM, Nielsen EJ, Park MA, Rumsey CL, Thomas JL, and Wood WA, *FUN3D Manual: 12.4*. NASA-TM-2014-218179 (2014).
6. Marcum DL and Weatherhill NP, *Unstructured grid generation using iterative point insertion and local reconnection*. AIAA Journal 33(9), 1619–1625 (1995).
7. Marcum DL, *Unstructured Grid Generation Using Automatic Point Insertion and Local Reconnection*. CRC Press (1998).
8. Bibb K, Gnoffo P, Park M, and Jones W, *Parallel, gradient-based anisotropic mesh adaptation for re-entry vehicle configurations*. AIAA 2006-3579 (2006).
9. Shenoy R, Smith MJ, and Park MA, *Unstructured overset mesh adaptation with turbulence modeling for unsteady aerodynamic interactions*. Journal of Aircraft 51(1), 161–174 (2014), doi: 10.2514/1.C032195.
10. Harris C, *Two-dimensional aerodynamic characteristics of the NACA 0012 airfoil in the Langley 8-foot transonic pressure tunnel*. TM 81927, NASA (1981).